To cite this version :

Experimental investigation of three-dimensional effects in cavitating flows with time-resolved stereo Particle Image Velocimetry

Kunpeng Long[1], *Olivier Coutier-Delgosha[1, 2], Annie-Claude Bayeul-Lainé[1]

[1]Laboratoire de Mécanique des Fluides de Lille – Kampé de Fériet, Arts et Métiers ParisTech, Lille, France

[2]Virginia Tech, Kevin T. Crofton Dept of Aerospace & Ocean Eng., Blacksburg VA 24060, USA

Abstract

The present paper is devoted to characterizing the three-dimensional effects in a cavitating flow generated in a Venturi-type profile. Experimental measurements based on 2D3C(Two-dimensional-three-component) stereoscopic PIV(Particle Image Velocimetry) are conducted to obtain the three components of the velocity field in multiple vertical planes aligned with the main flow direction, from the center of the channel to the side walls. Time-resolved acquisitions are conducted, so not only time-averaged quantities but also velocity fluctuations can be discussed. The attention was focused on configurations of cloud cavitation, where the attached cavity experiences large-scale periodical oscillations and shedding of clouds of vapor. Although the water channel is purely two-dimensional, some significant flow velocities in the third direction (depth of the test section) were measured. Some of them were found to be related to small differences between the boundary conditions on the two sides, such as minor gaps between the sides and the bottom wall, while others reflect intrinsic three-dimensional mechanisms inside the cavitation area, such as side jets that contribute to the periodical instability process. These mechanisms are discussed, and a possible 3D(Three-dimensional) structure of the cavitating flow is proposed.

**Keywords**: Cavitation, instability, flow imaging, PIV, 3D effects

---

* Corresponding author, ocoutier@vt.edu

1.Introduction

Although cavitation dynamics has been studied extensively in the last decades, using both experiments and computations, all the mechanisms in play in the instabilities generated by cavitating flows are far from being elucidated. One of the reasons is that even cavitation on simple bodies like two-dimensional profiles often exhibits complex behaviors, combining large-scale periodical shedding (called cloud cavitation) and high-frequency turbulent effects. The role of the re-entrant jet in the low-frequency flow instability has been shown for a long time[1, 2], but cases where a strong jet was observed, although no cloud cavitation was obtained, were also reported[3], while other mechanisms contributing to the instabilities were also discussed. For example, the role of bubbly shock propagation was highlighted by Ganesh et al. in 2017[4], and the presence of a strong Kelvin-Helmholtz instability at the cavity interface was shown recently by Podbevsek et al. 2021[5]. How these various processes combine and how much each of them triggers the flow unsteadiness are still open questions, and the responses likely depend on the flow conditions.

Even the flow organization is not clear, as its investigation is challenged by the fluctuations at various scales and the opaque nature of cavitation. High-frequency acquisitions are needed to access a time-resolved information: in the range of hundreds/thousands of Hz to capture the large-scale shedding, up to 100 kHz to track individual bubbles. It has induced, until recently, some strong limitations for non-intrusive optical techniques of investigation, such as Particle Image Velocimetry (PIV). Other limitations come from the difficulty of getting optical access to the areas of interest. Laser light sheets are distorted by the reflection of the beams on the bubble interfaces, and all bubbles between the laser light sheet and the camera form a mask that prevents any good quality measurement. Therefore, a lot of studies have been focused on the investigation of cavity wakes[6, 7] where the void fraction is low, boundary layers on the side walls[8], or just the liquid flow outside from the cavitation area[9].

The basic structure of the flow in a cavity attached to a solid wall was first described by Knapp et al. 1970[10] and later discussed in various publications: in the cavity closure, the external flow forms a jet impinging obliquely upon the wall. It results in two separate streams, one flowing upstream and later contributing to the cavity break-off, once it has reached the cavity front end, and the second one re-attaching to the wall downstream[11].
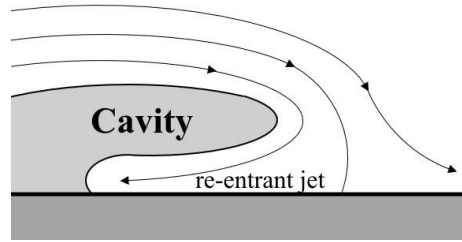
Figure 1. Schematic representation of the re-entrant jet flow in the closure region of an attached cavity

The re-entrant jet has been observed and measured several times using optical probes[12], electrical probes[13], laser-based PIV[14], and x-ray imaging-based PIV[3, 15]. Recent work by the present authors has revealed that this jet does not consist only of an intermittent negative speed in the main flow direction; instead, it has a more complex structure[16]. Measurements based on optical PIV in a small-scale venturi profile show that it is composed of a series of vortices generated at the cavity upstream end, which roll downstream and eventually form a step-shaped structure that will result in the cloud of vapor. This study suggests that significant three-dimensional effects, in addition to the purely 2D description of the cavity behavior, might play a role in the flow unsteadiness.

Studies focused on 3D effects can hardly be found in the literature. In an early theoretical study, Johnson(1961) combined solutions for several planar flows, using corrections derived from aerodynamics, to obtain a solution for a finite aspect ratio hydrofoil[17]. Numerical simulations are now providing 3D results, but a high level of inaccuracy still affects most of the calculations of cavitating flows. The global unsteady behavior of the cavity can usually be reproduced, as well as the time-averaged velocity fields, using advanced turbulence models like LES[18], but the local flow characteristics are often not consistent with the experimental data[19]. Nevertheless, Decaix & Goncalves have compared 2D and 3D simulations of cloud cavitation in a 2D venturi-type section, and they found that the 3D calculations provided a better agreement with the experimental data regarding the global frequency of the fluctuations, as well as the time-averaged velocity values in the flow direction and void fraction[20]. Some secondary structures generated in corners of the test sections were found in these simulations: a strong jet toward the center of the channel was observed, forming a vortex (see figure 2).
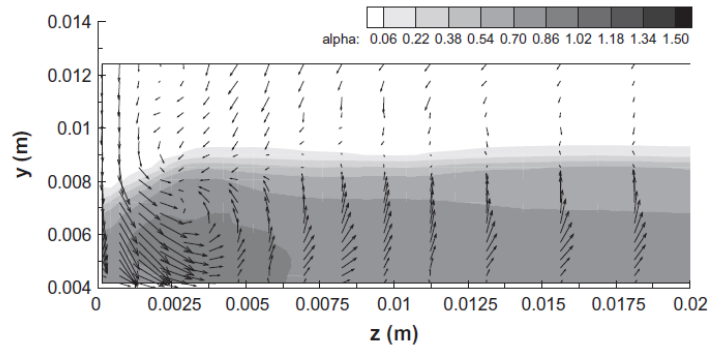
Figure 2. Snapshot of the void ratio and the velocity vectors in a transverse cutting plane, downstream of a venturi throat

On the experimental side, only a few notable studies have focused on the 3D structure of cavitation. Visualization from the side and the top was performed by Callenaere et al. in 2001, to observe the development of the reverse flow and the related events[11], but it did not provide any detailed information on the flow structure. More recently, Prothin et al. have recorded high-speed videos from the top of the cavity on a NACA0015 foil, and processed the data using POD and DMD. They observed a series of three-dimensional vortices formed by the lateral motion of the cloud of vapor[21]. However, the role played by these vortices in the mechanisms of the flow instability is not elucidated yet.

Indeed, experimental investigations of the 3D flow organization are challenging, as optical imaging, which is now the most usual technique of velocimetry in single-phase flows, is difficult to apply in cavitating flows. More specifically, Particle Image Velocimetry does not provide any accurate results in areas where the void fraction is higher than a few percent because of (i) the opacity of the liquid/bubbles mixture, which makes the particles, and (ii) the light reflection on the bubbles, which deforms the laser light sheet. The second effect can be drastically reduced by using fluorescent particles associated with notch filters on the cameras to record only the fluorescence emitted by the particles and filter the laser light. It has been used by several groups in the 2 last decades to measure the liquid velocities in areas of small void fraction, such as cavity wakes[9, 22, 23]. However, the first effect has no solution, unless the laser light sheet is located very close to one side wall, so that the fluorescence can be detected[14, 24]. This is the case when cavitation is studied at a small scale, like in Venturi-type sections of a few millimeters in depth and height[25]. In such a configuration, accurate 2D2C PIV results could be obtained and used to discuss the cavitation instabilities. Comparisons of
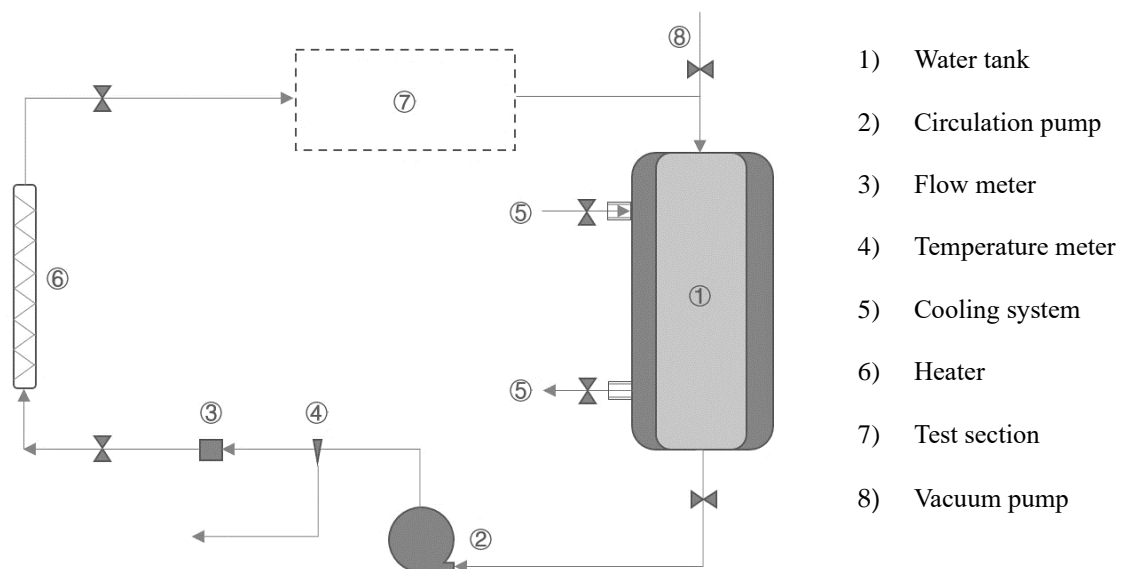
cavitating flows generated at different scales have shown that similar instabilities are obtained, although the quality of the finish of the surfaces is crucial at a small scale to avoid any side effect.

In the present study, cavitating flows in a small-scale 2D Venturi type section are investigated using 2D3C (two-dimensional – three components) PIV, in order to characterize the three-dimensional patterns specific to attached cavitation on a solid body. Section 2 presents the experimental setup and the measurement accuracy, while section 3 is focused on the flow structure, and section 4 is on the discussion of the results.

2. Experimental setup and measurements

2.1 Test Rig

Cavitation tests were conducted in a small-scale cavitation tunnel schematically represented in figure 3. This tunnel was designed for the particular purpose of velocimetry in a cavitating flow by ultra-fast X-ray imaging. All details related to the conception of the cavitation tunnel can be found in Khlifa et al.[15].

1)	Water tank
2)	Circulation pump
3)	Flow meter
4)	Temperature meter
5)	Cooling system
6)	Heater
7)	Test section
8)	Vacuum pump

Figure 3. Cavitation test facility

Water circulation is obtained with a Salmson-type Multi HE1602-SE-T/2-2G pump with variable rotation speed controlled by a micro-AC Variable Frequency Drive (VFD) model GS2-45P0 to set the flow rate. A tank partially filled with the circulation water is used for water cooling at the pump delivery to maintain a constant temperature, using a secondary cooling loop. The volume flow rate is measured by a Bürkert type SE32 (uncertainty 0.15 l/min after in situ calibrations) turbine flow meter. Temperature is obtained with a type K thermocouple, directly in contact with circulation water.

Upstream from the test section, a noise attenuation device is used to filter the periodical pressure fluctuations due to the passage of the pump blades. The reference pressure is measured 10 mm upstream from the venturi test section with a Series 6M/S(C) OEM pressure transducer connected to an EV 94 EB digital indicator. The uncertainty on the measurements was of the order of 50 Pa. Another pressure meter measures the downstream pressure 10mm downstream from the test section. The partially filled tank is connected to a compressor and a vacuum pump, which enables variation in the pressure in this tank between 0.1 bar and 3.5 bar, thus adjusting the pressure in the test section.

2.2 Venturi-type Section

The geometry of the test section is similar to the one used previously at a larger scale by Stutz and Reboud at a larger scale to characterize the re-entrant jet in cloud cavitation[1] or Dular et al. to perform PIV measurements close to the side walls[26]. Here, a small-scale version of the Venturi profile is used, like in our previous experiments based on X-ray imaging[15, 27].

The main body of the test section is 3D printed, while the bottom, top, and side walls of the convergent/divergent nozzle are inserts made of transparent optical glass (figure 4). The venturi shape (bottom wall) is a simple wedge: the flow is accelerated in the convergent part of the venturi, which has an 18° angle. The maximum speed at the throat (width 5 mm, height 10 mm) is in the range of 10 to 20 m/s. Cavitation is initiated immediately downstream from the edge of the Venturi, which has an 8° divergence angle, and it collapses abruptly as the fluid moves outwards since the pressure re-increases downstream.
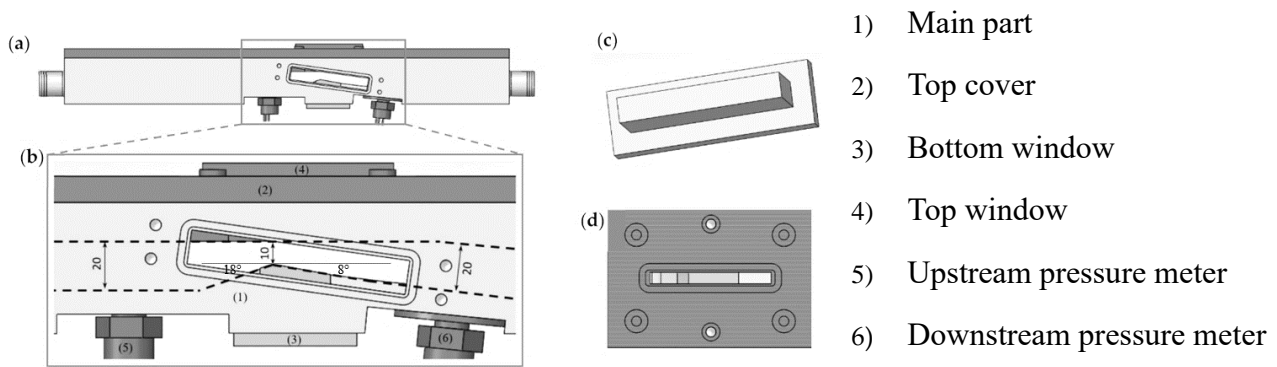
Figure 4. Venturi-type section: (a, b) side views, (c) side window, (d) top window

1) Main part
2) Top cover
3) Bottom window
4) Top window
5) Upstream pressure meter
6) Downstream pressure meter

2.3 PIV measurements

The flow field is illuminated from the top with a vertical light sheet generated with a DM150-532-DH dual-head Nd: YAG laser from Photonics Industries (figure 5). The light sheet is about 1 mm thick and is located in the middle of the test section. The flow is seeded with PMMA-RhB-Frak Fluorescent tracers with an average 10 μm diameter, which re-emit light at a 584 nm wavelength significantly higher than the original 527 nm of the laser.

Two Phantom v2512 high-speed cameras were used to capture simultaneous images from one side of the test section, as shown in figure 5. The cameras are equipped with notch filters that eliminate the wavelengths around 527 nm in order to capture only the light emitted by the particles. It enables the removal of the reflections of the laser light on the cavitation bubbles while capturing the images of particles. The bright spot generated by each particle is typically 20 to 50 μm, i.e., 1 to 2 pixels on the images. Note that it is about 2 to 5 times the size of the particles only, as the spot is due to the fluorescence emitted by the particles, not the reflection of the incident light, so the halo generated by each particle is significantly smaller.

The two cameras are oriented with an angle of around 25 to 30 degrees from the direction perpendicular to the windows, which was found to be the best compromise between the accuracy of the velocity 3rd component and the sharpness of the images.
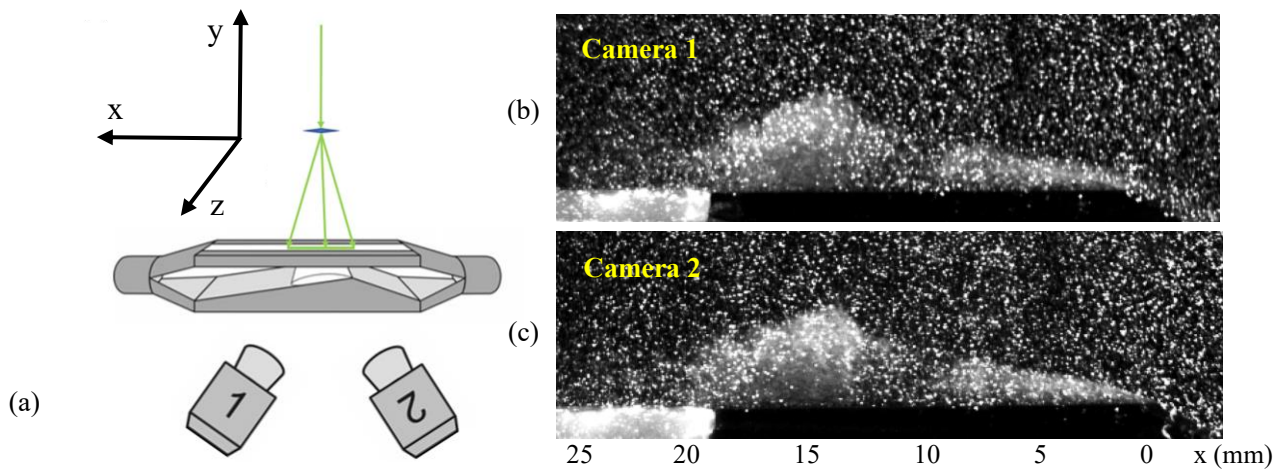
Figure 5. (a) scheme of the PIV setup, (b, c) Raw images of particles obtained simultaneously with the two cameras

For each flow condition, 20,000 8-bit pictures with a resolution of 768 x 480 pixels were recorded by the two cameras with an exposure time of about 200 ns (duration of the laser flash). These 20,000 pictures are composed of 10,000 times two frames separated by 5 µs, acquired at a frequency of 25,000 Hz in order to time resolve the motion of the vapor structures in the flow field. So the total time of acquisition is 0.4s. The 5 µs time between the two frames corresponds to a typical displacement between 0.5 and 2 pixels in most of the flow field, which is smaller than the usual prescriptions for PIV, but enabled in this specific case to minimize the uncertainties.

The cameras and the laser were synchronized with a high-speed controller, and the images were recorded using the Davis LaVision 10.0 software.

To perform measurements in the different vertical planes in the z-direction (see figure 5), the test section is mounted on a sliding frame controlled with a micrometric screw of precision 0.01 mm, to adjust precisely the laser light sheet position from the front side to the backside (5 mm distance with 0.5 mm between two successive positions). This setup enables moving only the test section without changing anything in the PIV setup. Note that the test section was fixed rigidly to the frame so that only the entire frame could slide, but no other motion was enabled, which was critical for the accuracy of the calibration.

A thorough calibration process was performed once the laser light sheet, camera fields of view, and image sharpness were adjusted: the test section was moved so that the light sheet was at the middle of the channel, then the top (see figure 3b) was open to the air, but still maintained full of

water. A micro calibration plate from LaVision (200 µm distance between the dots, covering the 30×10 mm^2 surface of the field of view) was inserted into the test section and used to record the calibration data. The micrometric screw was used to move the test section to the front and back for the stereo PIV calibration. Once the process was completed, the test section was closed for measurements.

2.4 Test cases

Four flow conditions were investigated, as reported in Table 1. Only the flow rate Q was changed, while the pressure in the downstream tank was maintained at atmospheric pressure. It results in 4 values of the cavitation number $\sigma = \left(P_{up} - P_v\right)/\frac{1}{2}\rho V_{th}^2$, where V$_{th}$ is the mean speed at the Venturi's throat, P$_{up}$ is the pressure upstream from the test section, P$_v$ is the vapor pressure, and ρ is the liquid density.

|	Temp (°C)	Pv (Pa)	ρ (kg/m3)	Vth (m/s)	Q (l/min)	Area (mm²)	σ	Pup (Pa)	Pdown (Pa)
1	23	2807	997.541	15	45	50	1.19	136500	98800
2	23	2807	997.541	16	48	50	1.06	138000	98100
3	23	2807	997.541	17	51	50	1.00	147000	97300
4	23	2807	997.541	18	54	50	0.95	156500	96600

Table 1. Investigated cavitation conditions

For each flow condition, 9 laser sheet positions in the z direction were investigated, from 0.5mm off the back side window(P1) to 0.5mm off the front side window (P9).

2.5. PIV post-processing

To enhance the quality of the images of particles inside the cavitation areas, a pre-processing was applied to eliminate, as much as possible, the traces of the cavitation bubbles. It is based on particle brightness standardization and background filter, and it enabled to obtain a quite uniform brightness of the particles in the entire flow field (see figure 6).

The vector fields are calculated from the images of particles using the Davis 10.0 software from LaVision. Interrogation areas of 64×64 pixels with 50% overlap are applied for the first 2 passes, and then 16×16 pixels windows with 75% overlap for the last 3 passes. Vectors with a correlation factor lower than 0.6 or a Q factor lower than 1.3 were removed from the results. The final results are

smoothed by applying a 3×3 Gaussian kernel.
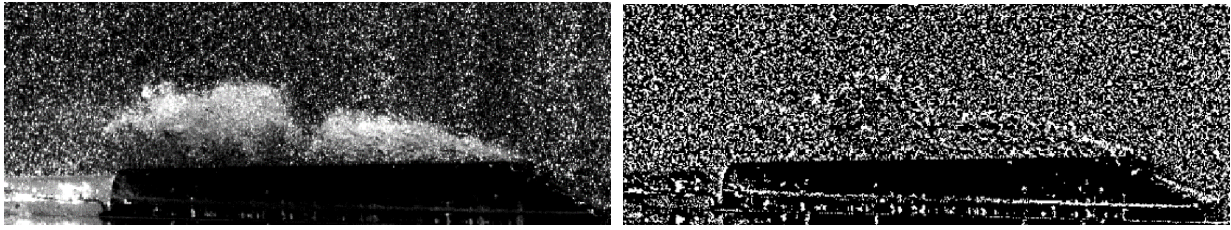
**Figure 6**. Raw image of particle (left) and processed image used for PIV (right)

Figure 7 displays the typical distributions of correlation factors, peak ratios, and uncertainty obtained for the three components of the velocity in test case #4. Note that it is shown here at a given time, for the sheet cavity shown in figure 7f, but the levels remain very similar for all PIV results obtained in this experiment. The uncertainty on V_x is systematically smaller than 2% in the entire field of view, while the one on V_y is smaller than 1%. Higher values are obtained for V_z, with peaks in the range of 4 to 5%, but most of the data still have an uncertainty lower than 3%. In addition, the correlation factors are always higher than 0.7, and the peak ratio is always higher than 2.

This level of accuracy, which is consistent with previous PIV campaigns performed on the same geometry with a different system working at lower frequency[16] is considered good enough to analyze hereafter the three-dimensional structure of the flow field and discuss the impact of the 3D effects.
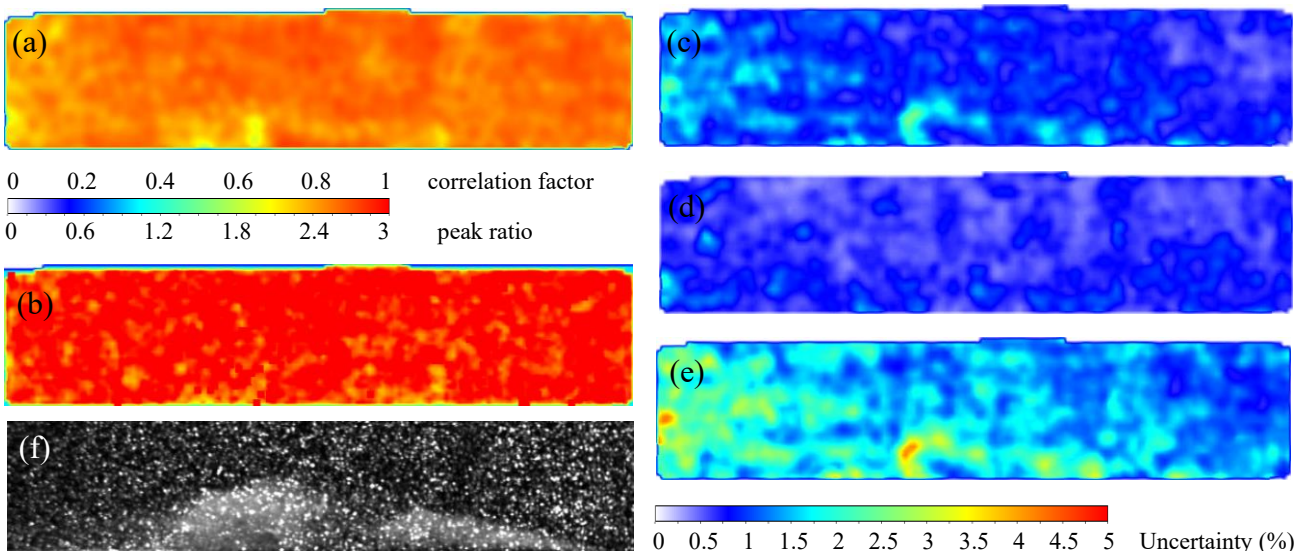
Figure 7. Typical distributions of (a) correlation factor, (b) peak ratio, (c, d, e) uncertainty on V_x, V_y, V_z in test case #4, for the sheet cavity indicated in (f).

The quantity of image pairs to be used to calculate the time-averaged velocity fields was selected based on a convergence study shown in figure 8. Two specific locations are considered here: (a) inside the cloud of vapor, once it is detached from the attached cavity, and (b) inside the attached cavity, in the area where the re-entrant jet is flowing upstream. In both cases, a satisfactory convergence was obtained on V_x and V_y with about 6000 pairs of images, while 8000 is required for V_z. Therefore, 10,000 pairs of images were eventually used for all time-averaged velocity fields used hereafter to discuss the 3D structure of the flow field.
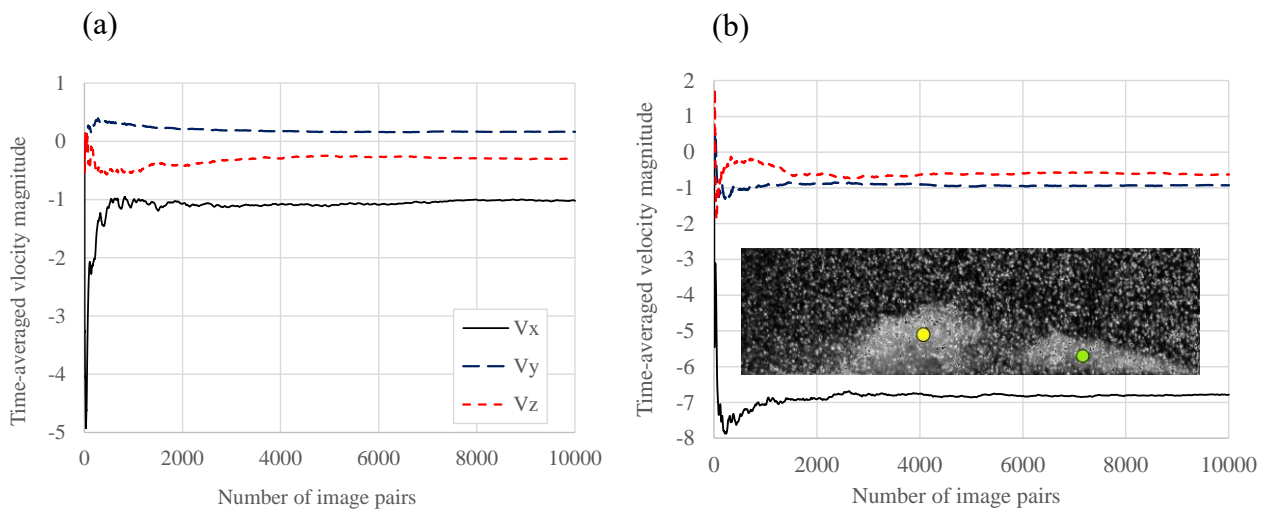
Figure 8. Convergence of the time averaged velocity components according to the number of image pairs: (a) at the location of the cloud detachment (yellow dot), (b) in the re-entrant jet (green dot).

3. Results

3.1 General unsteady behavior

The flow behaviors observed in the present experiment are the same as those described in a previous paper by Long et al.[16], with three different types of sheet instabilities: (1) single cloud cavitation, (2) multi-clouds cavitation, and (3) sheet cavitation.

For small-size sheet cavities, type (3) is dominant, with random shedding of small clouds of bubbles in the wake of the cavitation area, but no clear periodic detachment. It is associated with a very weak re-entrant jet at the bottom wall, which can hardly flow up to the upstream end of the

cavity. For larger sheet cavities, periodical shedding of large-scale clouds of vapor is obtained, with four distinct steps (cavity growing, cavity up-lift, cavity break-off, cloud convection) described in detail by Long et al.[16]. The re-entrant jet plays a crucial role in that process, as can be seen in figure 9, which shows the typical four stages of the cavity (images a to d).

Figure 9a shows the growing stage, where a continuous cavitation region is formed downstream from the Venturi's throat. The Vx velocity component (color field), as well as the velocity vectors, show a thin re-entrant jet flowing upstream along the bottom wall (note that positive Vx values here correspond to the re-entrant jet), forming a series of vortices in the bottom half of the sheet cavity (not shown here). This series of vortices gradually merge while the thickness of the re-entrant jet increases, forming a bulge-like structure, as shown in figure 9b (up-lift stage). When this bulge grows to a certain level, the re-entrant jet weakens in between the bulge and the upstream end of the sheet cavity, enabling the main flow to cut it and separate the cavitation area into two sections (figure 9c). The detached cloud is then pushed and rolled downstream under the combined actions of the main flow and the re-entrant jet.

During the up-lift stage, when the re-entrant is strong, multiple bulges can form, resulting eventually in several points of separation between these bulges at the next stage. In that case, several cavitation clouds are generated and detach almost simultaneously: this is the multi-clouds cavitation configuration shown in figure 9e. The raw image shows here three independent cavitation clouds, which are rotating counterclockwise. The Vx distribution also shows that the re-entrant jet is cut into three sections. The evolution of this configuration is less predictable than the single cloud cavitation case: sometimes the clouds will move downstream individually and collapse separately, and sometimes they will merge together and be convected as a single cloud.

In the flow conditions indicated in Table 1, the flow sometimes oscillates between two configurations, typically between sheet cavitation and single cloud cavitation or between single and multiple cloud cavitation for larger cavities. The investigation of the 3D effects in the present study is performed in the specific case of single cloud cavitation, so we have selected acquisitions where this configuration is dominant.
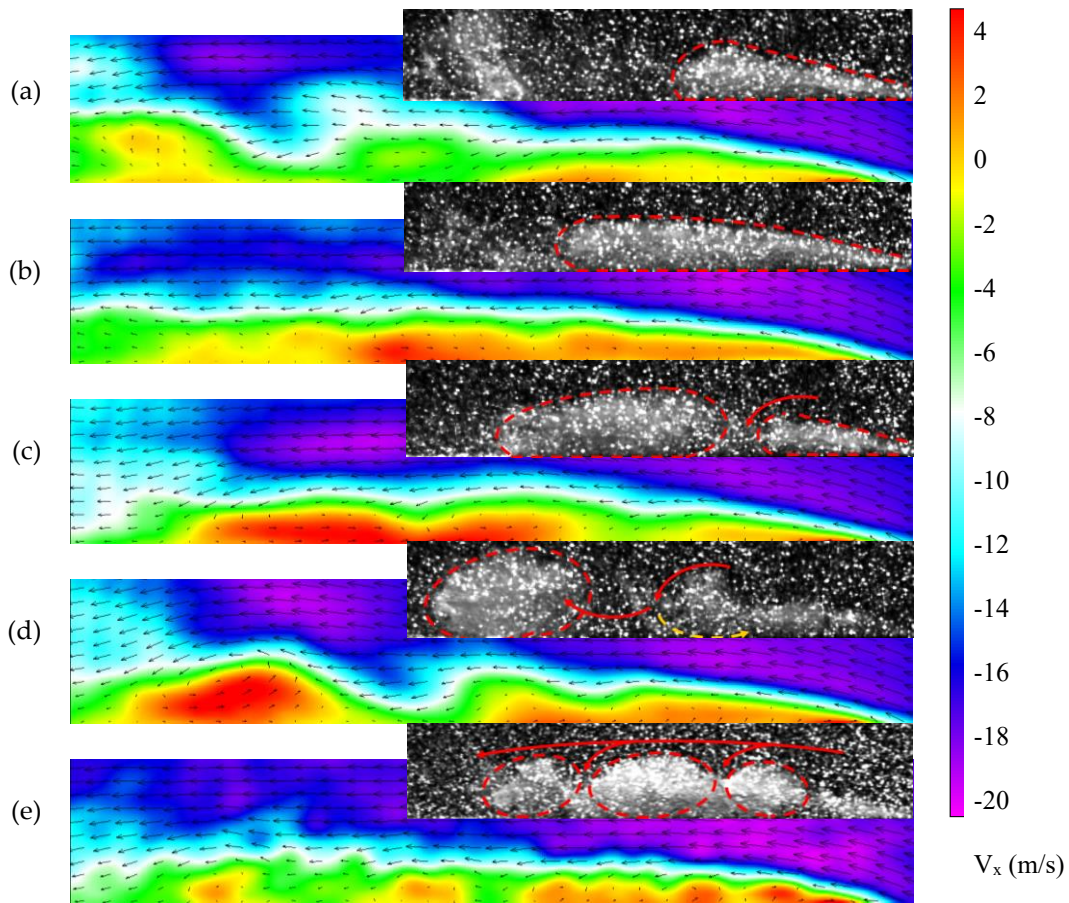
Figure 9. Raw images and instantaneous velocity component Vx (color field) superimposed with the velocity vectors for the 4 steps of single cloud cavitation (a) cavity growing, (b) cavity up-lift, (c) cavity break-off, (d) cloud convection. (e) Cavity break-off in case of multiple clouds

The examination of the z-component of the instantaneous velocity fields reveals a very complex fluctuating behavior, with characteristic frequencies close to the frequency of the cloud shedding (see figure 10). It suggests that the flow instability generates some significant perturbations in the z-direction, related to the cavity break-off and the rolling of the cloud of vapor, which is also certainly strongly coupled with the turbulence. The study of these effects is out of the scope of this work since the velocity fields were not acquired simultaneously in the 9 vertical planes, so the instantaneous 3D structure of the flow is not available. The study is thus intentionally focused on the large-scale dominant three-dimensional effects induced by cavitation, so only the time-averaged velocity fields will be used hereafter.
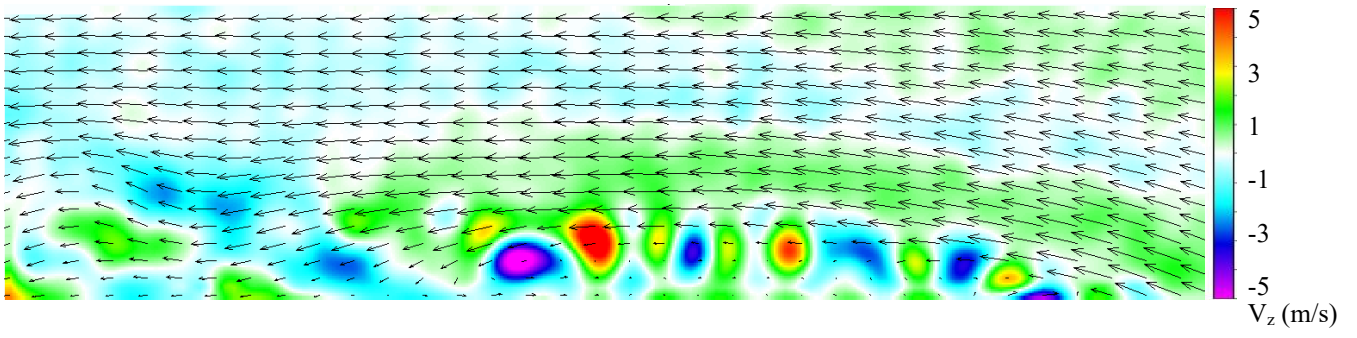
Figure 10. Instantaneous Vz distribution for test case #4 in the middle of the channel

3.2 Variation in the z direction

The flow in the venturi-type section is primarily two-dimensional. Figure 11 shows the time-averaged gray level brightness of the images of cavitation (left) in the nine vertical planes between the two sides of the test section (called hereafter P1 to P9), as well as the time-averaged vorticity distribution (middle). No significant variation according to z can be detected: only a decay of the general brightness with the distance to the observation window (from P9 to P1) can be observed, but no change in the vorticity is noticed.
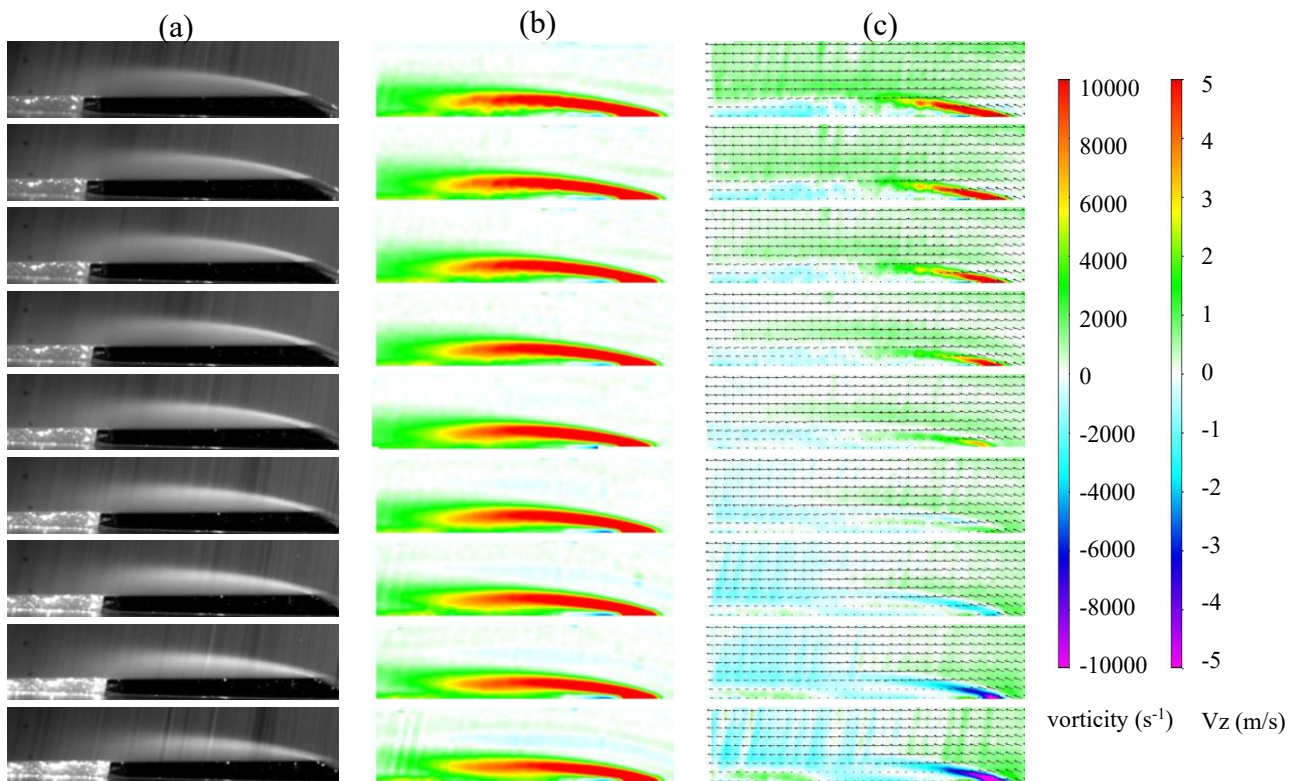
**Figure 11**. a) Time-averaged brightness of the raw images, b) Time-averaged vorticity field, c) Time-averaged Vz – Test case #4, positions 1 (back) to 9 (front) from top to bottom

This qualitative similarity is confirmed by the quantitative comparisons displayed in figures 12a, b, and c, regarding the maximum vorticity in the height of the channel from x = -5 mm to x = 25 mm, the maximum Vx component (i.e., the max speed of the re-entrant jet), and the minimum Vx (i.e., the max. speed of the main flow). A pretty close agreement between the 9 different planes is obtained for these three parameters, which means that the dynamics of the flow are very similar at all z positions.

However, the examination of the z component of the velocity also reveals some significant 3D effects: figure 11c shows that a significant Vz velocity affects the upstream part of the sheet cavity,

with negative speeds in the front (positions P6 to P9) and positive speeds in the back (positions P1 to P5), meaning that the flow is moving from the sides to the center of the channel. This is confirmed by figure 12d, which shows the evolutions of the maximum V_z in the channel height from x = -5 mm to 25 mm. An intense side jet characterized by a maximum amplitude of 7 m/s on both sides is present at the upstream end of the cavity, before decreasing progressively more downstream.
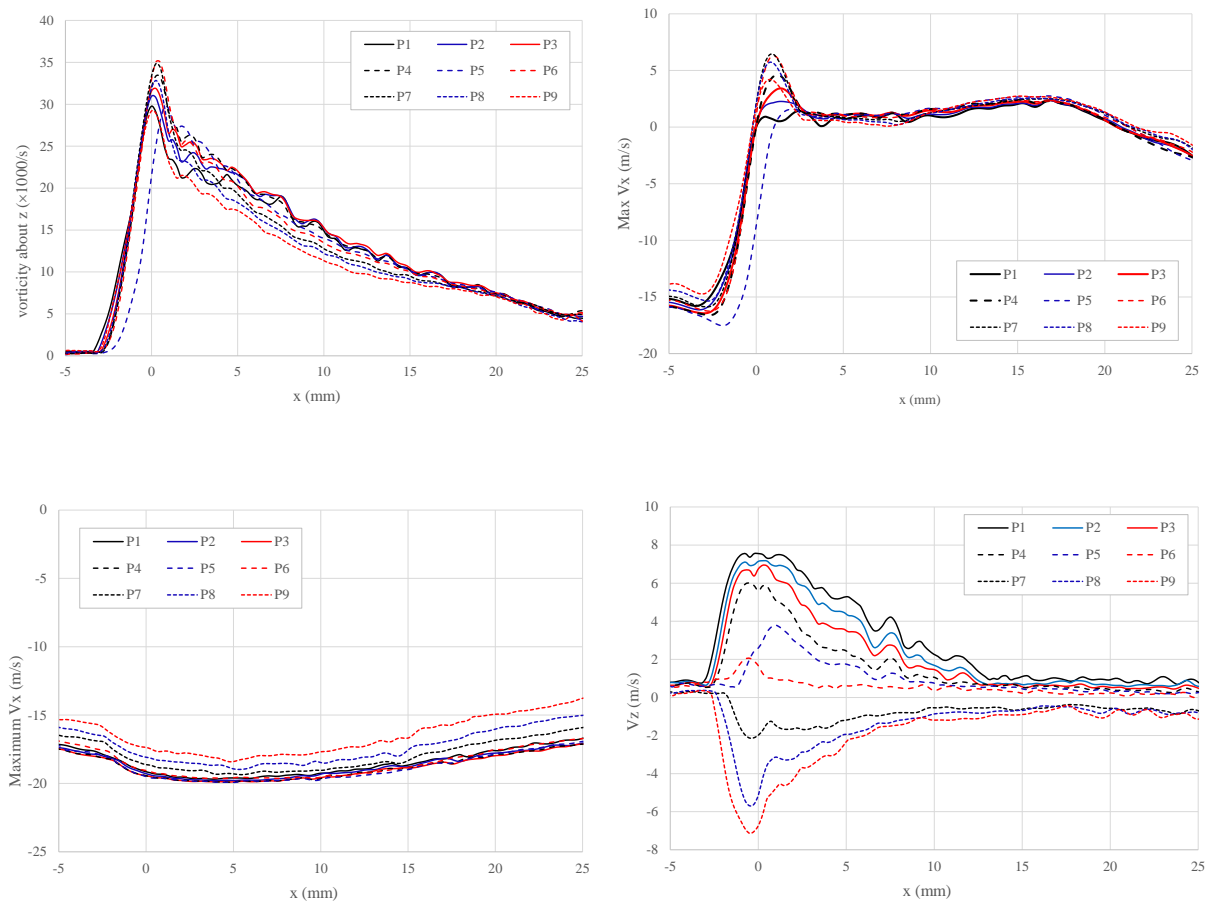
Figure 12. Evolution according to x of (a) the max. vorticity along the z axis, in the height of the channel, (b) the max. V_x component (re-entrant jet), (c) the minimum V_x component (maximum speed of the main flow), (d) the max. V_z component. The results are shown in the 9 vertical planes, from P1 (back side) to P9 (front side).

To get a better understanding of the flow structure in the z-direction, figure 13 displays for test cases 1 to 4 the z evolution of four quantities calculated in the nine vertical planes P1 to P9: the mean V_x, the mean V_z, the re-entrant jet max. speed, and the max. V_z magnitude. It shows that both the main flow and the re-entrant jet have a higher speed in the middle of the channel, compared to the sides: the variation is quite small for the main flow (of the order of 20% of the max. speed), but it is

larger for the re-entrant jet (close to 50% of the max. speed). This is observed for the 4 flow conditions. Both the mean V_z and max. V_z evolutions confirm the presence of the jet towards the center of the test section, with intensity decreasing quite linearly from the sides to the center. Note that all results here show an asymmetry of the channel, as the zero mean V_z is obtained at position P7, the max. V_z is minimal at position P6, and the re-entrant jet max. speed is minimal at position P6 as well. Globally, the flow is quite symmetrical apart from position P6, while the center of the channel is at position P5. This might be related to a small imperfection at the junction between the side windows and the bottom wall, inducing a spurious side effect that slightly shifts the symmetry plane to the front.
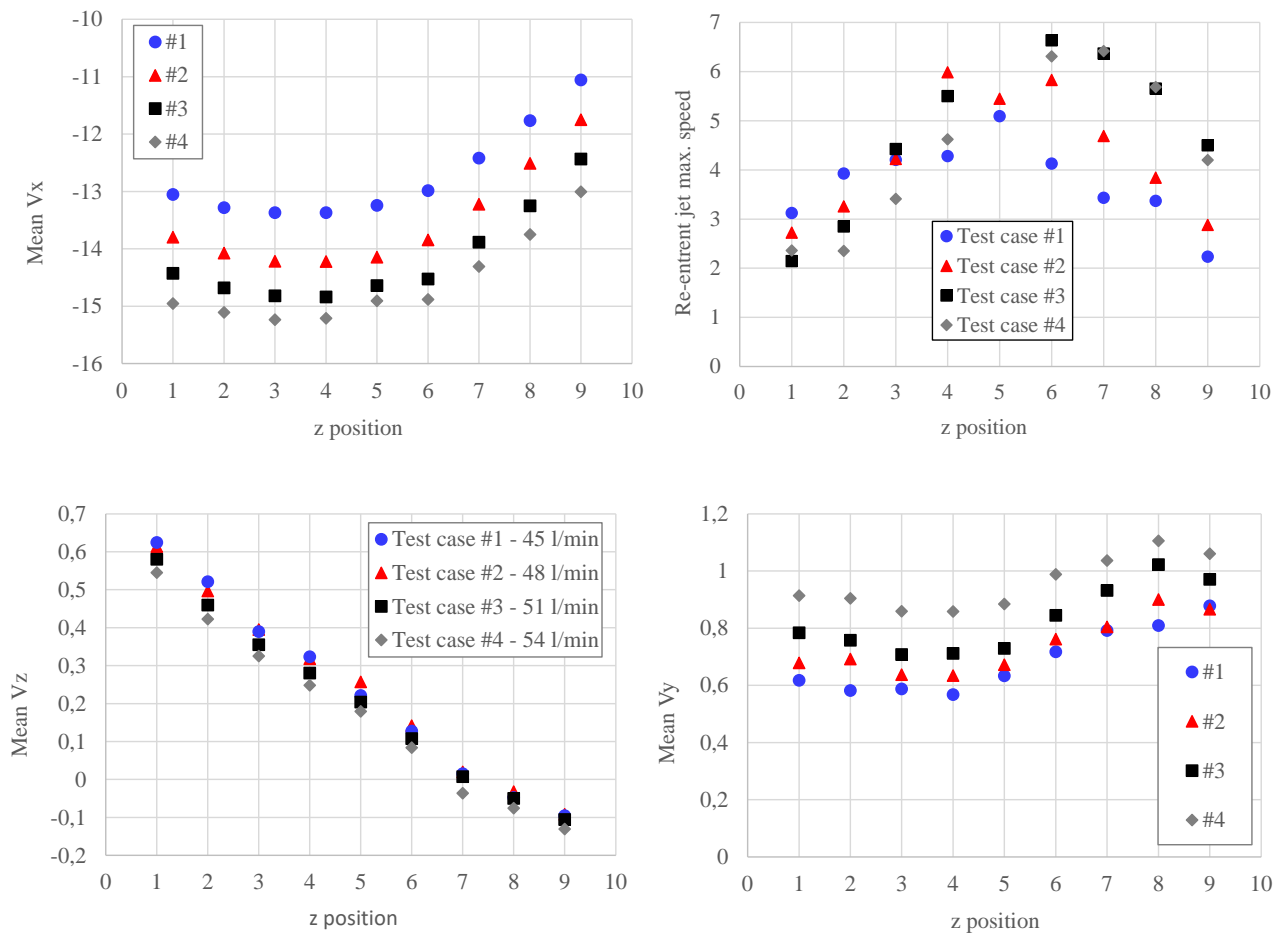
Figure 13. Evolution in the z direction of (a) the mean V_x in the x-y plane located at z, (b) the re-entrant jet max. speed in the x-y plane located at z, (c) The mean V_z in the x-y plane located at z, (d) the max. V_z in the x-y plane located at z

3.3 Three-dimensional structure

In order to better understand the 3D flow structure close to the bottom wall, in the re-entrant jet

region, velocity vectors calculated in test case #4 are plotted in figure 14 in several x-z horizontal planes located at several heights above the Venturi surface, with the V_x velocity component as background color field. The horizontal axis is the position in the x direction (remember the venturi throat is at x = 0), and the vertical axis is the position in the z direction from the backside (z = 0.5mm) to the front side (x = 4.5 mm).

The re-entrant jet (positive V_x values) is most intense immediately above the bottom wall (y = -2.1 mm) at two distinct x positions. The first one is just downstream of the throat (1 < x < 3 mm), where the jet reaches a maximum speed of approximately 7.5m/s (the empty area at the center of the channel is due to missing data close to the bottom wall, because of the mask used for PIV data processing). This high-speed reverse flow enables the sheet cavity to stay attached and grow, until the cloud eventually detaches. The second region of intense reverse flow is located between x = 10 and 17 mm, downstream from the break-off position, right below the detached cavity cloud. This second patch, where the maximum speed is approximately 3m/s, is related to the rolling of the cloud of vapor in the counterclockwise direction after it is shed.

At higher y positions, the intensity of the re-entrant jet decays rapidly, particularly in the area immediately downstream from the throat. At y = -1.4mm, the velocity of the entire re-entrant jet is close to zero, which means that the thickness of the re-entrant jet is approximately 0.7 mm at this flow condition. However, it must be reminded that all velocities here are time-averaged. The horizontal plane at y = -0.7 mm is characterized by alternate negative and positive velocities, depending on the steps of the periodical cycle of vapor shedding, which results in time-averaged speeds close to zero. So this region of the flow is still part of the re-entrant jet dynamics.

At higher y positions, the re-entrant jet is not present anymore at all, but the speed is still significantly lower than the one of the main flow. This one is recovered at approximately y = 1 mm (see figure 15).

The right part of figure 14 displays a vertical z-y plane located at x = 2 mm immediately downstream from the throat. The horizontal axis is the z direction from P1 to P9, and the vertical axis is the y direction. It shows that the entire re-entrant jet region represents only a small part of the venturi cross-section, but the dynamics in this small part trigger most of the properties of the sheet

cavity.
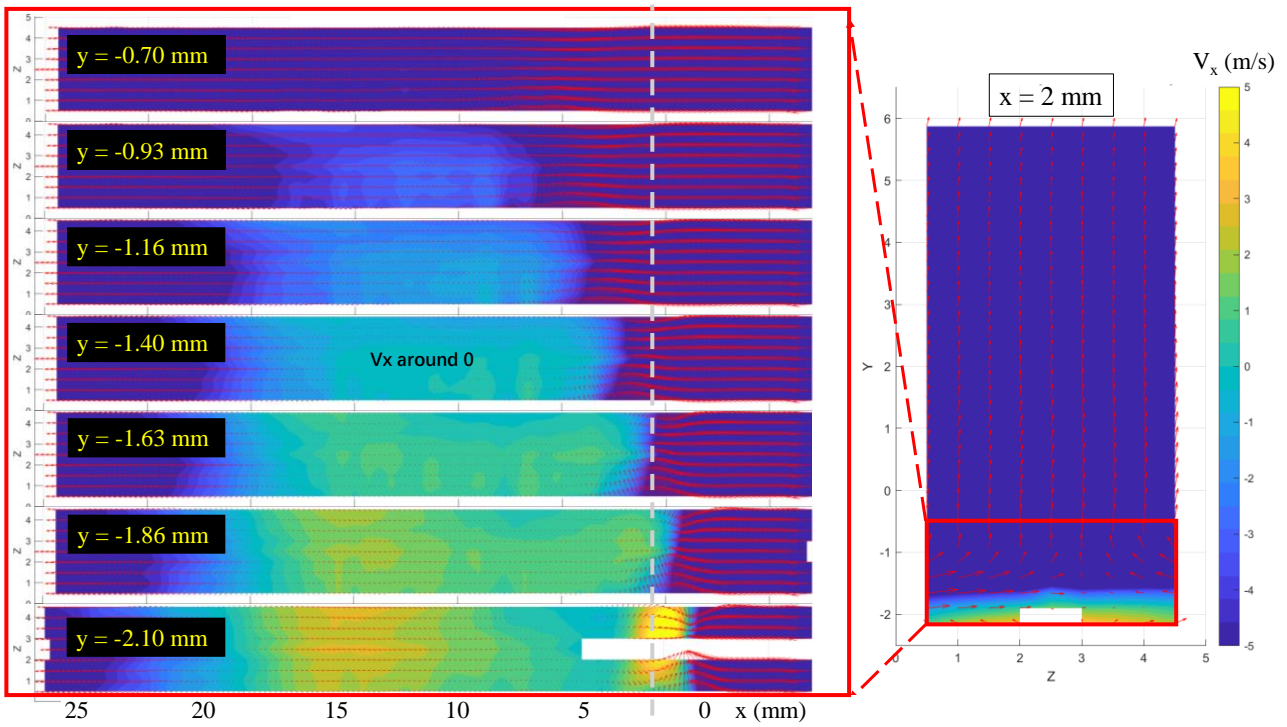
Figure 14. Left: time-averaged velocity vectors in x-z planes at different y positions within the re-entrant jet with V_x as background color field; Right: time-averaged velocity vectors in the z-y plane located at x = 2 mm, with V_x as background color field (test case #4)
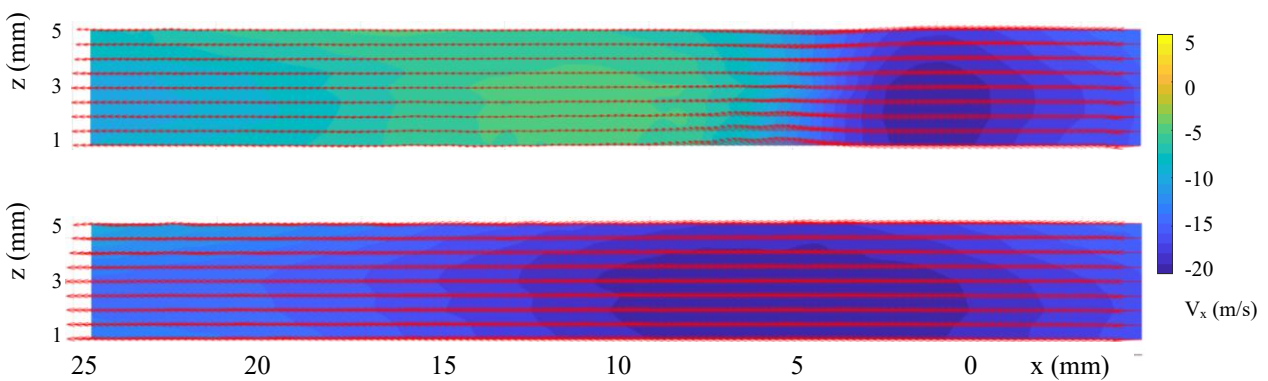
Figure 15. Time-averaged velocity vectors superimposed with Vx (color field) in the x-z plane located at y = -0.7 mm (top) and y = 1 mm (bottom) for test case #4

Details of the flow field immediately downstream from the throat (-3 < x < 5 mm) are displayed

in figure 16. It shows that while it vaporizes, the flow is pinched to the center of the channel, and it also goes up to get around the sheet cavity. The speeds directed to the center are definitely larger at the back side, compared with the front, which results in a junction of the two side flows at z between 3 and 3.5 mm (between P6 and P7), as observed previously in the mean V_z evolution. Conversely, the re-entrant jet is more intense in the front, since the momentum is more directed to the x direction, instead of being partially moved to the side.
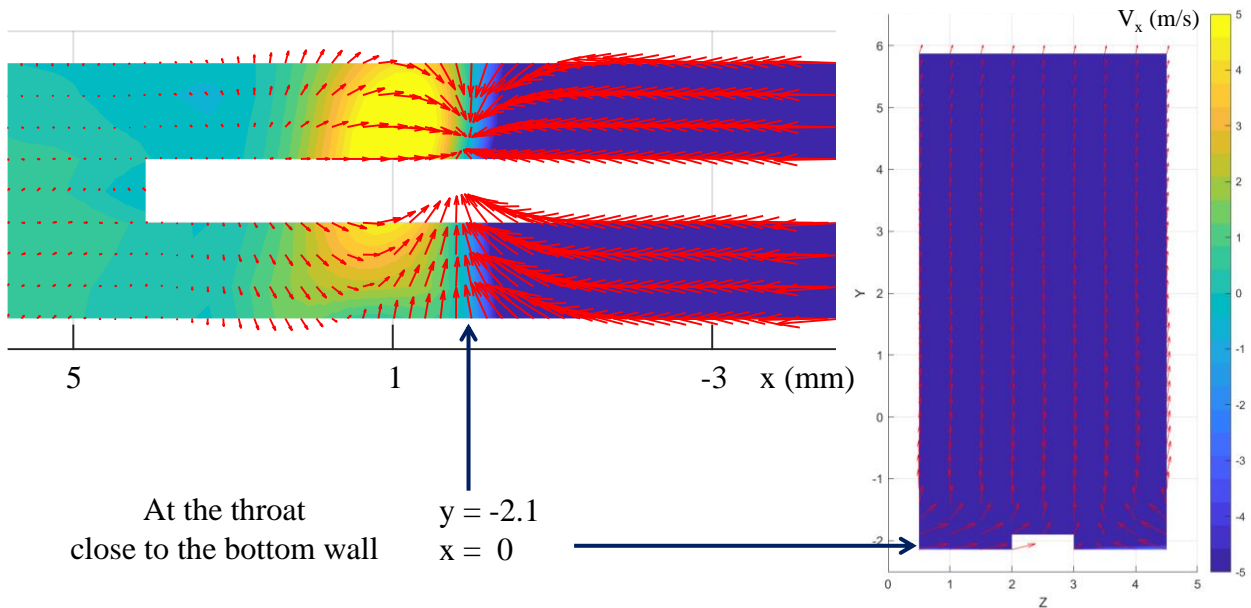

Figure 16. Zoom at the flow field close to the bottom wall, immediately downstream from the throat: velocity vectors and Vx (color field) in the x-z plane located at y = -2.1 mm (left) and in the y-z plane located at x = 0 (right) for test case #4

In figure 17, the velocity vectors are plotted in 5 different y-z planes located at distances from 0 to 10 mm from the Venturi's throat. It shows that the side jet is essentially located at the interface between the attached sheet cavity and the mainstream region, slightly above the re-entrant jet. Therefore, the more we move downstream, the more the side jet is found at higher y positions. At the same time, a rapid decay of its intensity is observed.
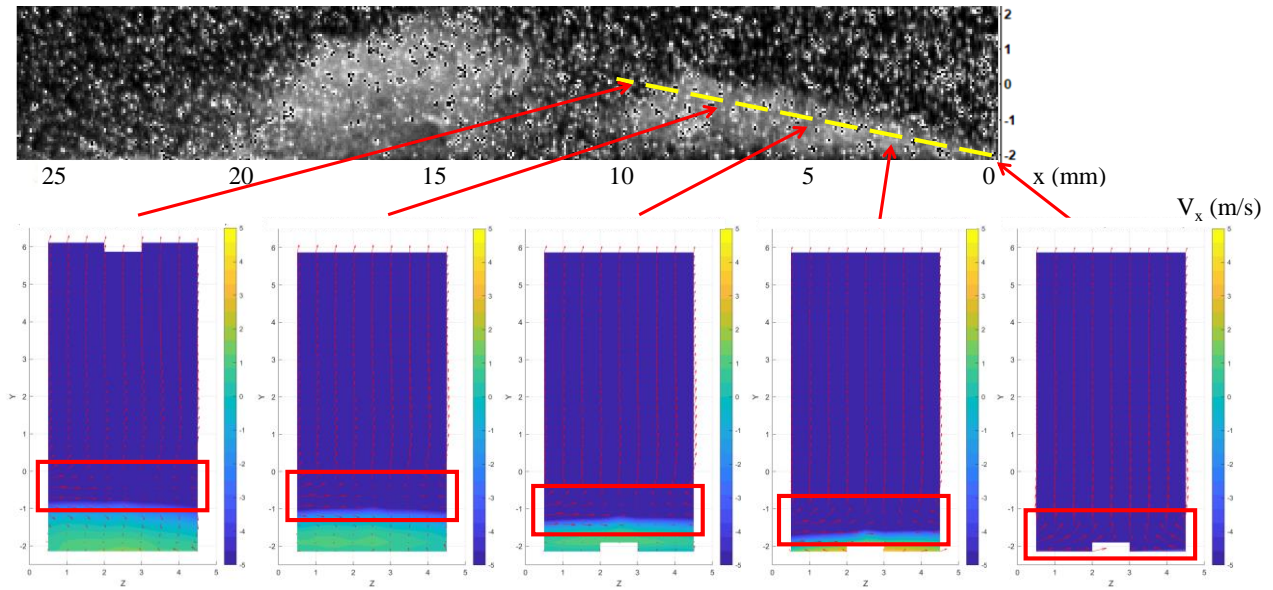
Figure 17. Time-averaged velocity vectors in y-z planes located at different x positions downstream from the throat with V_x as background color field (test case #4)

This side jet has not been detected in previous experiments or simulations[20, 28], possibly because the 3D simulations often assume periodical conditions at the side walls, rather than boundary layers that require a very costly mesh refinement. In the present experiments, it has not been found in non-cavitating flow conditions, while it starts to be observed when cavitation grows on the wall (sheet cavitation configurations). In cases of cloud cavitation studied here, the intensity of the side jet does not vary significantly with the flow rate (and thus the size of the sheet cavity), as indicated in figure 18a. It leads to the preliminary conclusion that this phenomenon is directly related to the unsteady mechanisms of vapor shedding, through the re-entrant jet dynamics at the cavity leading edge.
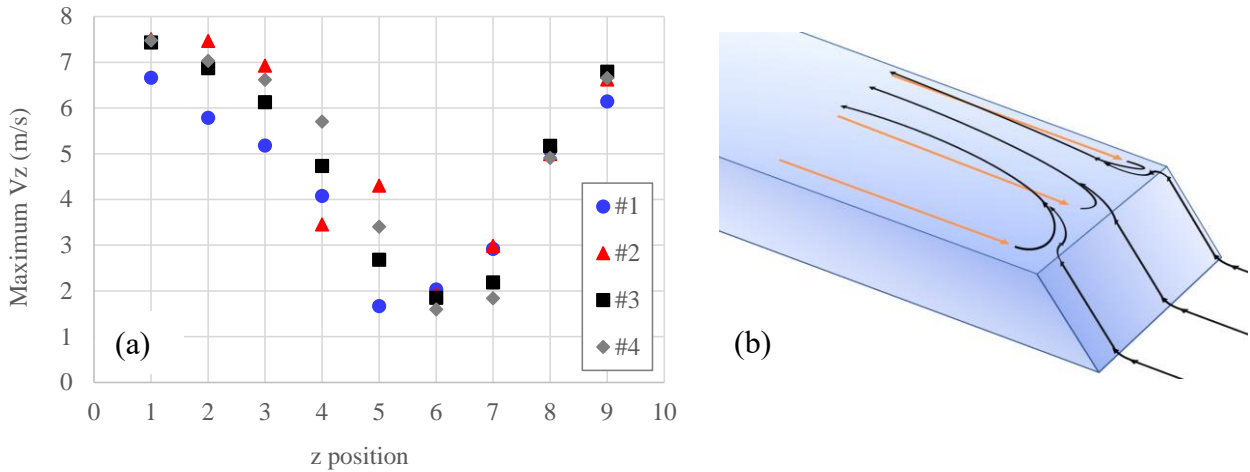
Figure 18. (a) Max. time-averaged velocities of the side-jet in planes P1 to P9, for the 4 test cases, (b) 3D schematic of the flow at the Venturi throat.

Based on this analysis, a three-dimensional schematic of the flow inside the attached sheet cavity, immediately downstream of the throat, is shown in figure 18b. The incoming flow at the throat, as it faces the re-entrant jet coming from downstream, is submitted to a side jet from the sides to the center, generated by the turn of the re-entrant jet, which still has some momentum. The flow is also lifted in the same process, thus accelerating the speed at the sheet cavity top interface. This effect of local flow acceleration at the top of the cavitation region has already been observed in previous experiments focused on the velocity fields in x-y planes[3, 15, 27].

More downstream, in the area where the cavity break-off usually happens, the side jet, although it has lost some intensity, has also developed more in height: figure 19 shows that for x close to 12 mm (last y-z plane on the right), a large part of the y-z cross sections is submitted to a significant V_z velocity, still from the sides to the center. This velocity is directed partially downward into the re-entrant jet region, and partially upwards into the mainstream region. It also shows that the re-entrant jet intensity is quite low at this position (the max. V_x speed is around 1 m/s), which suggests that the side jet coming from above is significantly disturbing it, eventually leading to the cut of the sheet cavity and its break-off, as described in section 3.1.
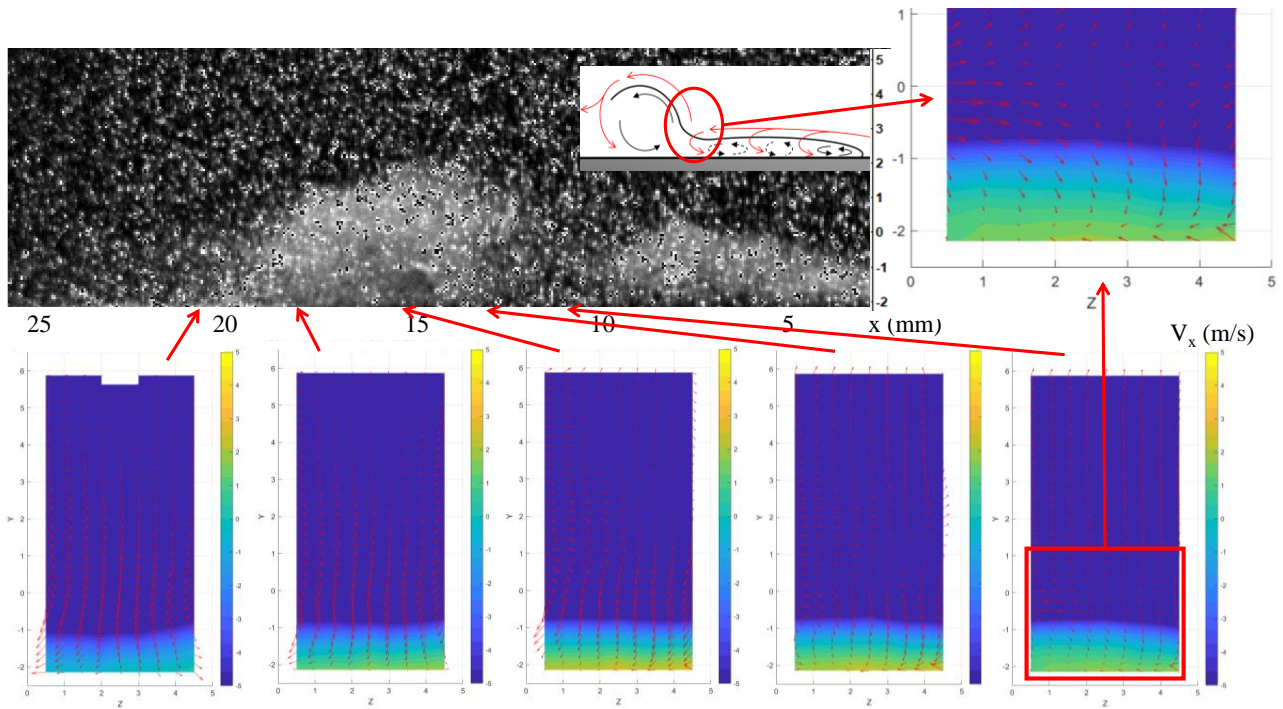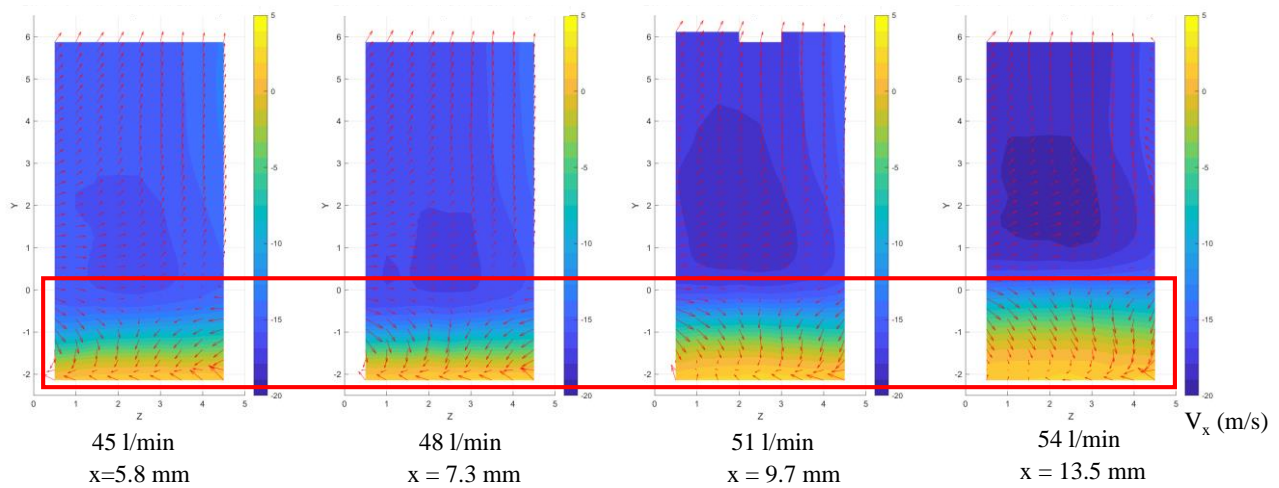
Figure 19. Time-averaged velocity vectors in y-z planes located at different x positions downstream from the cavity break-off location, with V_x as background color field (test case #4)

It was shown by Long et al.[16] that the cavity break-off is due to the formation of a bulge in the rear of the attached cavity, under the action of the re-entrant jet that lifts the bulge into the main flow region, causing the pressure to rise in front of it, resulting in cutting the connection between the bulge and the cavity sheet where the re-entrant jet is weaker. Eventually, this process initiates the cloud shedding. Thanks to the three-dimensional velocity field obtained here, this cut of the cavity can be visualized. The x position of the phenomenon varies in each test case, due to the different cavitation lengths, however, the flow field structure is generally the same, as shown in figure 20. It consists of a strong flow resulting from the side jet, flowing mostly downwards and also toward the center of the channel. This fluid impacts the re-entrant jet, and will divide into two streams, as will be seen later: one merging with the reverse flow in the attached cavity, the other one flowing underneath the detached cloud.
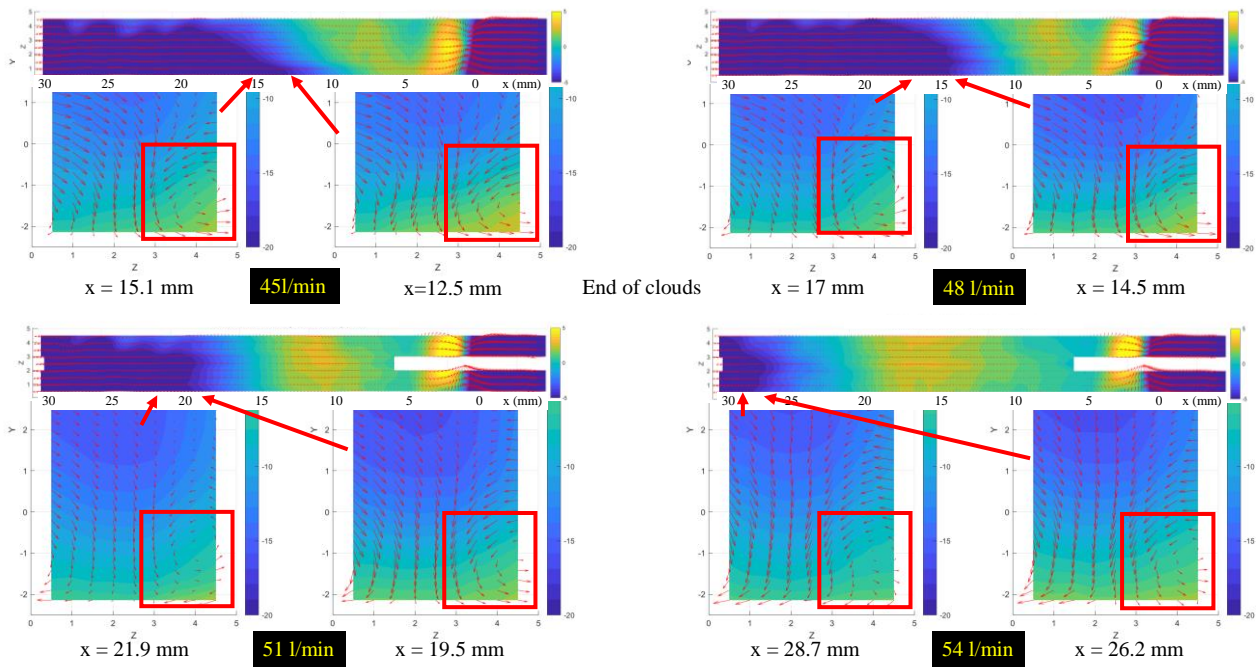
Figure 20. Time averaged velocity vectors and V_x color field in y-z planes located at the x position of the cavity break-off, for test cases 1 to 4 (left to right).

Further downstream, for x between 13 and 20 mm (see the 4 y-z planes on the left of figure 20), the situation becomes more complex, with a flow from the sides to the center and simultaneously to the bottom in the top part of the channel, and a flow from the center to the sides at the bottom. The more downstream we go, the more downwards the flow in the entire cross-section. This range of x positions in test case #4 is where the detached cloud of vapor is present, so this flow structure can be related to the spin of the cloud along the z-axis in the counter clock direction. In the rear part of the cloud, all velocities are from top to bottom, while at the front, a significant part above the re-entrant jet is going up.

Further downstream, once the re-entrant jet has vanished, a counter-clockwise vortex is visible in the lower right corner of the y-z cross-section, near the bottom wall and the side windows, as shown in figure 21 for the different test cases. For test case #4, this vortex is located at x = 27 to 29 mm, i.e., roughly at the location of the collapse of the cloud of vapor. It can be seen that a similar pattern tends to be created in the lower-left corner, so it can be assumed that if the channel was perfectly symmetrical, two identical vortices would be obtained, with a clockwise rotation in the left corner. This secondary flow suggests that the cloud of vapor is characterized by a 3-dimensional rotation during its collapse, counter-clockwise in the x-y plane and both clockwise and counter-clockwise in the y-z plane, on the two sides. Figure 22 shows a schematic of the flow organization downstream

from the cavity break-off (note that the orange arrow shows the re-entrant jet).

Figure 21. Time-averaged velocity vectors in y-z planes downstream from the cavity break-off, for the 4 test cases. The color field shows V_x.
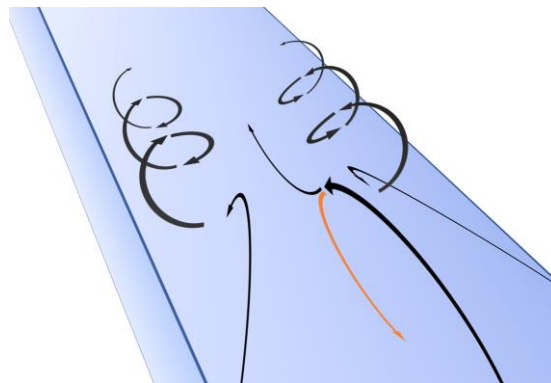

**Figure 22**. Schematic of the flow organization, downstream from the cavity break-off location

4. Discussion

In this section, our objective is to use the data presented hereabove to propose an explanation for

the 3D features of the flow field, especially the inception of the side jet at the sheet cavity leading edge. As shown previously in figure 16, this jet starts to appear immediately downstream from the throat as the incoming flow interacts with the re-entrant jet. It develops at the interface between the main liquid flow area and the re-entrant jet (figure 23), which is an area of high velocity and pressure gradient, where intense vaporization is observed and confirmed by previous x-ray imaging in a similar flow configuration (figure 24).
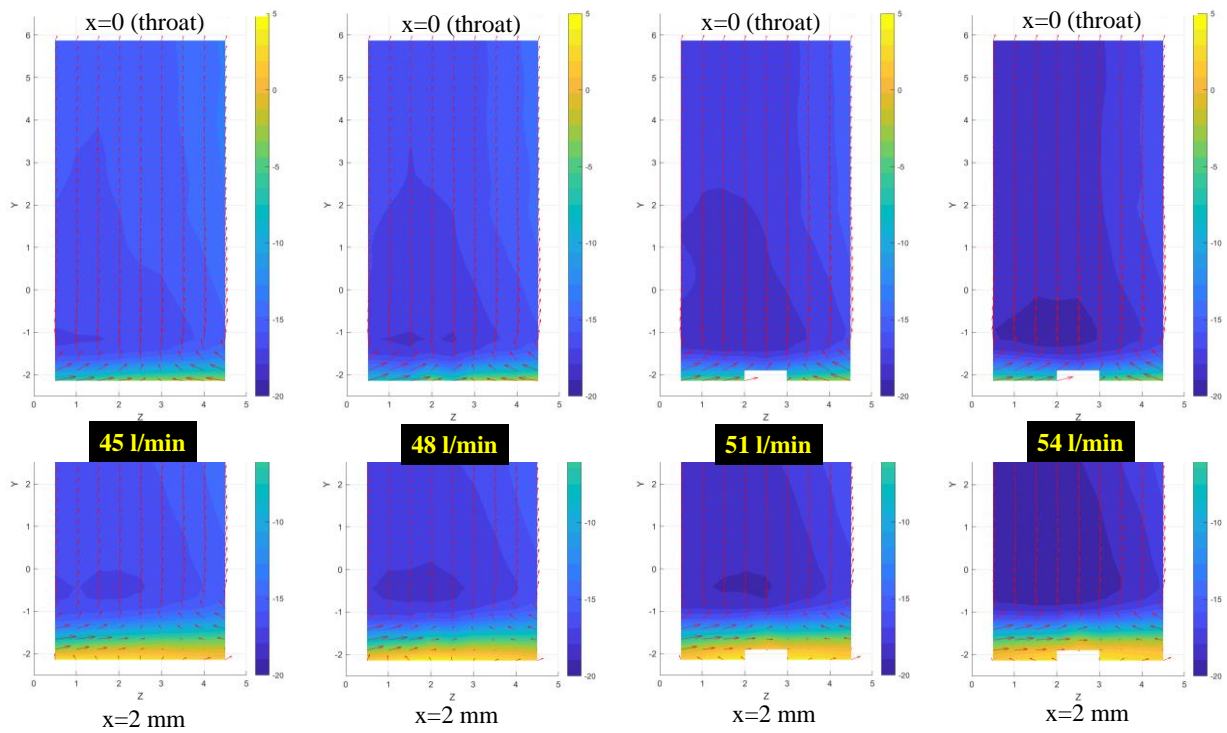

**Figure 23**. Side jet structure in y-z planes for different flow condition with Vx as background color
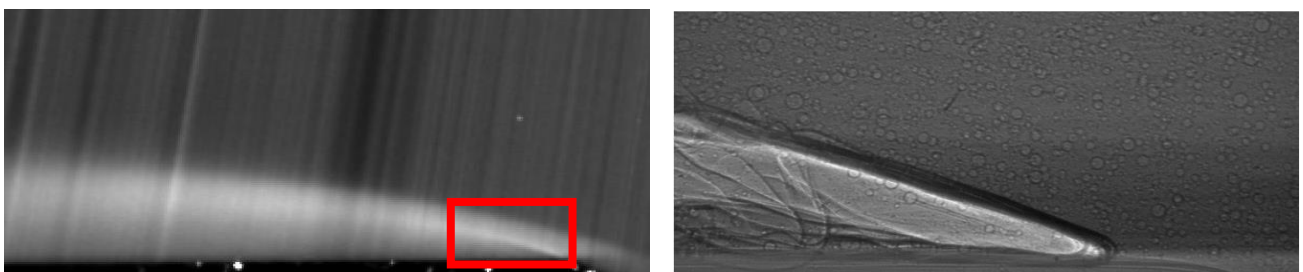
Figure 24. (a) Time-averaged brightness of raw images for test case #4 (position P9), (b) x-ray visualization of the intense vaporization at the cavity upstream end, in the same Venturi.

At the Venturi's throat, due to the 18° convergence angle and the 8° divergence angle, the incoming flow is deflected by an angle of 26°, so V_y decreases accordingly, and V_x also decreases due to the expansion of the Venturi flow channel (figure 25). However, the intense vaporization delays the velocity reduction caused by the expansion of the flow path. So, the combination of the cavity's fast expansion, the large V_x speed of the incoming flow, the significant momentum of the re-entrant jet, and the presence of the walls at the bottom and on the sides direct the flow up and to the center of the channel, generating a diagonal jet towards the interface. Downstream, as the vaporization rate is lower and the V_x speeds decrease, the strength of the side jet also decreases, as described in the previous section.
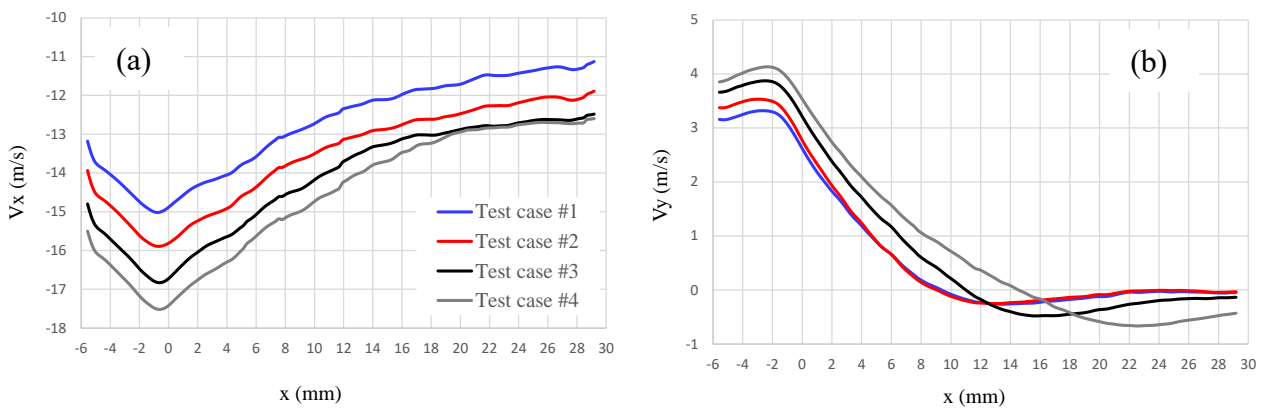
Figure 25. Time-averaged mean velocity (a) V_x in y-z vertical planes, according to x, (b) V_y in x-z horizontal planes, according to y

As mentioned previously, the flow field and the side jet are non-symmetrical. The effect is obtained in all test conditions for the 3 components of the velocity, and it is not related to any inaccuracy in the measurements. It was found that a small gap between one of the side windows and the bottom wall was responsible for this specific effect. Indeed, any side gap as small as 0.1 mm (while the test section is 5 mm wide) was found to generate a significant asymmetry, like the one observed in the present results. This is clearly a limitation in the use of a small-scale test section, although it must be mentioned that quite strong side effects, impacting sometimes the overall cavitation behavior, have been reported in the past also at a larger scale[29].
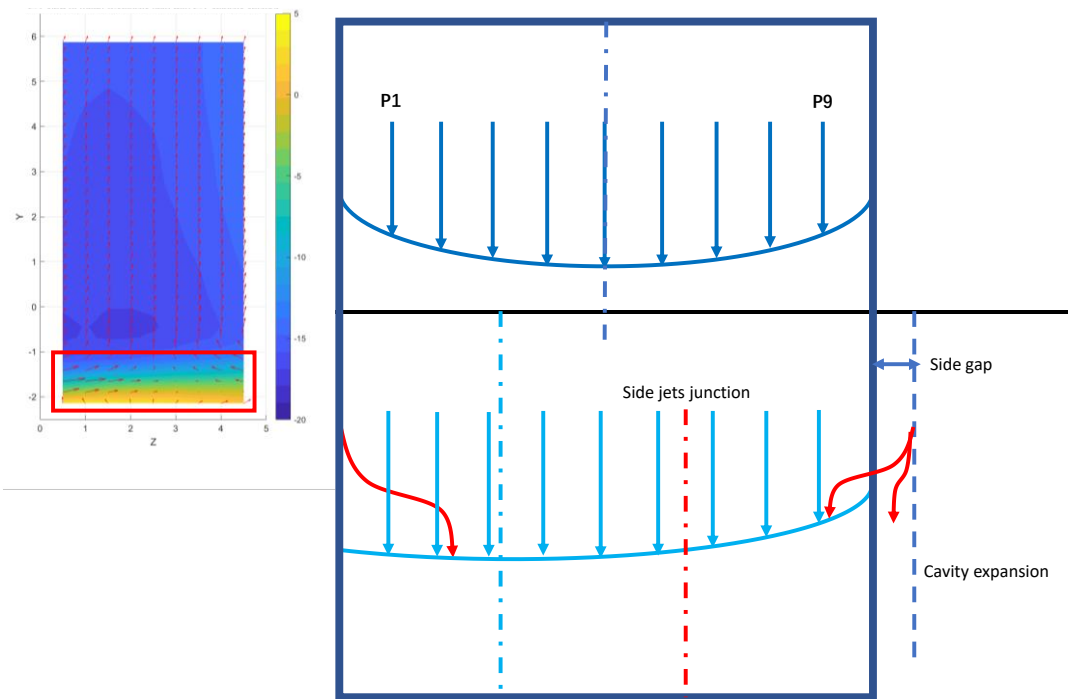
Figure 26. Schematic of side-gap and side-jet effects

Under normal conditions, if the incoming flow is uniform and stable, the flow field should be symmetrical, as shown in the upper part of figure 26, with two identical boundary layers on the sides and the side jet that would enhance the difference of speed between the center and the sides. However, it was shown in section 3 that the axis of symmetry of the V_x velocity component is between the P3 and P4 positions (see the mean V_x or V_y in figure 13). This asymmetry also impacts the side-jet intensity, which is higher on the P1 side and lower on the P9 side, but the axis of symmetry (where V_z equals 0) is between P6 and P7 (figure 18). The same is observed for the re-entrant jet (see figure 13). This asymmetry can actually be used to confirm our hypothesis: the side where the re-entrant jet is the strongest is also the one that generates the most intense side flow.

5. Conclusion

In this paper, an analysis of the 3D flow structure inside the cavitation area generated on a 2D Venturi profile was studied using 2D3C PIV. The three components of the time-averaged velocity field were studied in various y-z planes from the leading edge to the downstream end of the sheet cavity, and in x-z planes located at various heights from the bottom surface to the junction to the pure liquid flow. A strong jet from the sides to the center, was detected in the area of intense vaporization

just downstream from the Venturi's throat. This jet goes up towards the cavity top interface with the liquid main flow, contributing to the local acceleration detected in previous studies at the sheet cavity interface. It was shown that this jet resulted from the deviation of the incoming flow induced by the re-entrant jet, which is turning as it reaches the throat: the stronger the reverse flow, the larger the flow deviation to the center.

More downstream, this side jet goes down, due to the higher pressure generated at the front of the "bulge" induced by the lift of the rear part of the attached cavity (detailed by Long et al.[16]), eventually cutting the cavity at positions where the re-entrant jet is the weakest, and thus causing the cavity break-off and the detachment of a large-scale cloud of vapor.

Additional mechanisms were reported downstream of the cavity break-off, due to the rotation of the cloud of vapor in the counter-clockwise direction. Two vortices rotating along the x-axis were identified on the sides of the cloud, generating a complex three-dimensional structure. Overall, some significant three-dimensional mechanisms were detected, some of them directly contributing to the flow instability, although the flow configuration is purely 2D.

Author's Contribution

Kunpeng Long: Experiments, Data analysis, Writing of the original draft
Annie-Claude Bayeul-Lainé: co-supervision of the work
Olivier Coutier-Delgosha: Supervision of the work, Writing, review & editing.

Data Availability

Data available on request from the authors. The data that support the findings of this study are available from Kunpeng Long (kunpeng.long@ensam.eu), upon reasonable request.

References

1   Stutz B, Reboud J L. Experiments on unsteady cavitation[J]. Experiments in fluids, 1997, 22(3): 191-198.

2   Callenaere M, Franc J P, Michel J M, et al. The cavitation instability induced by the development of a re-entrant jet[J]. Journal of Fluid Mechanics, 2001, 444: 223-256.

3   Zhang G, Khlifa I, Fezzaa K, et al. Experimental investigation of internal two-phase flow structures and dynamics of quasi-stable sheet cavitation by fast synchrotron x-ray imaging[J]. Physics of Fluids, 2020, 32(11): 113310.

4   Ganesh H, Mäkiharju S A, Ceccio S L. Bubbly shock propagation as a mechanism of shedding in separated cavitating flows[J]. Journal of Hydrodynamics, Ser. B, 2017, 29(6): 907-916.

5   Podbevšek D, Petkovšek M, Ohl C D, et al. Kelvin-Helmholtz instability governs the cavitation cloud shedding in Venturi microchannel[J]. International Journal of Multiphase Flow, 2021, 142: 103700.

6   Gopalan S, Katz J. Flow structure and modeling issues in the closure region of attached cavitation[J]. Physics of fluids, 2000, 12(4): 895-911.

7   Arndt R E A, Song C C S, Kjeldsen M, et al. Instability of partial cavitation: a numerical/experimental approach[J]. 2000.

8   Dular M, Bachert B, Stoffel B, et al. Relationship between cavitation structures and cavitation damage[J]. Wear, 2004, 257(11): 1176-1184.

9   Foeth E J, Van Doorne C W H, Van Terwisga T, et al. Time resolved PIV and flow visualization of 3D sheet cavitation[J]. Experiments in Fluids, 2006, 40(4): 503-513.

10   Knapp R T, Daily J W, HAMMITT F. G. 1970 Cavitation[J]. McGraw-Hill Book Company, London.

11   Callenaere M, Franc J P, Michel J M, et al. The cavitation instability induced by the development of a re-entrant jet[J]. Journal of Fluid Mechanics, 2001, 444: 223-256.

12   Stutz B, Reboud J L. Experiments on unsteady cavitation[J]. Experiments in fluids, 1997, 22(3): 191-198.

13   Pham T M, Larrarte F, Fruman D H. Investigation of unsteady sheet cavitation and cloud cavitation mechanisms[J]. 1999.

14   Dular M, Bachert R, Stoffel B, et al. Experimental evaluation of numerical simulation of cavitating flow around hydrofoil[J]. European Journal of Mechanics-B/Fluids, 2005, 24(4): 522-538.

15   Khlifa I, Vabre A, Hočevar M, et al. Fast X-ray imaging of cavitating flows[J]. Experiments in fluids, 2017, 58(11): 1-22.

16   K. LONG, Coutier-Delgosha O, et al. Analysis of the cavitation instabilities with time-resolved stereo and multiplane Particle Image Velocimetry

17   Johnson V E. Theoretical and experimental investigation of supercavitating hydrofoils operating near the free water surface[M]. National Aeronautics and Space Administration, Scientific and Technical Information Office, 1961.

18   Gnanaskandan A, Mahesh K. Large eddy simulation of the transition from sheet to cloud cavitation over a wedge[J]. International Journal of Multiphase Flow, 2016, 83: 86-102.

19   Apte D, Ge M, Coutier-Delgosha O. Comparison of Reynolds shear stress methods for RANS turbulence modelling of a cloud cavitation in a venturi[C]//APS Division of Fluid Dynamics Meeting Abstracts. 2021: P28. 008.

20   Decaix J, Goncalves E. Investigation of three-dimensional effects on a cavitating Venturi flow[J]. International Journal of Heat and Fluid Flow, 2013, 44: 576-595.

21   Prothin S, Billard J Y, Djeridi H. Image processing using proper orthogonal and dynamic mode decompositions for the study of cavitation developing on a NACA0015 foil[J]. Experiments in fluids, 2016, 57(10): 1-25.

22　Gopalan S, Katz J. Flow structure and modeling issues in the closure region of attached cavitation[J]. Physics of fluids, 2000, 12(4): 895-911.

23　Kravtsova A Y, Markovich D M, Pervunin K S, et al. High-speed visualization and PIV measurements of cavitating flows around a semi-circular leading-edge flat plate and NACA0015 hydrofoil[J]. International Journal of Multiphase Flow, 2014, 60: 119-134.

24　Dular M, Bachert R, Schaad C, et al. Investigation of a re-entrant jet reflection at an inclined cavity closure line[J]. European Journal of Mechanics-B/Fluids, 2007, 26(5): 688-705.

25　Ge M, Zhang G, Petkovšek M, et al. Intensity and regimes changing of hydrodynamic cavitation considering temperature effects[J]. Journal of Cleaner Production, 2022, 338: 130470.

26　Dular M, Khlifa I, Fuzier S, et al. Scale effect on unsteady cloud cavitation[J]. Experiments in fluids, 2012, 53(5): 1233-1250.

27　Ge M, Zhang G, Nematikourabbasloo N, et al. Application of fast synchrotron X-ray imaging in velocimetry of cavitating flows[C]//SNAME 26th Offshore Symposium. OnePetro, 2021.

28　Barre S, Rolland J, Boitel G, et al. Experiments and modeling of cavitating flows in venturi: attached sheet cavitation[J]. European Journal of Mechanics-B/Fluids, 2009, 28(3): 444-464.

29　Gouin C, Junqueira-Junior C, Goncalves Da Silva E, et al. Numerical investigation of three-dimensional partial cavitation in a Venturi geometry[J]. Physics of Fluids, 2021, 33(6): 063312.